JOURNAL OF GEOPHYSICAL RESEARCH, VOL. 94, NO. B10, PAGES 13,739–13,754, OCTOBER 10, 1989

MANTLE HETEROGENEITIES, GEOID, AND PLATE MOTION: A MONTE CARLO INVERSION

Yanick Ricard, Christophe Vigny, and Claude Froidevaux

Département de Géologie, Ecole Normale Supérieure, Paris

Abstract. Seismic tomography in both the upper and the lower mantle, as well as subducting oceanic slabs defined by seismicity, has been translated into density heterogeneities to generate models of mantle circulation. These models can predict both the surface velocities and the geoid, which can be compared with plate tectonics and gravity data. A given model is specified by 6 parameters related to the viscosities of 3 mantle layers and the absolute amplitudes of density variations in the upper and lower mantle as well as in the slabs. The values of these parameters are chosen at random within an acceptable range. Each model is submitted to an appropriate test comparing observations with predictions. The results of the most successful models selected by this Monte Carlo inversion are displayed. They yield preferred mantle viscosity structures exhibiting large variations at depth. With a physical interface between upper and lower mantle, i.e., with the possibility for the circulation to penetrate the 650 km discontinuity, two classes of viscosity profiles stand out. The first one implies a regular increase of the viscosity in the sublithospheric mantle, with reasonable values for the density parameters. The second one is unexpected in the sense that it predicts a very stiff bottom for the upper mantle. It also requires vanishingly small amplitudes for the upper mantle density heterogeneities defined by tomography, which would thus have to be of lithological rather than thermal origin. With a chemical interface at 650 km the outcome is very similar: the same two classes of viscosity structures do yield a satisfactory geoid prediction. However only the class of models with a stiff layer at midmantle depths predicts acceptable surface velocities. Altogether the best models out of some 60,000 which have been tested only explain one third of the geoid and two thirds of the surface divergence for spherical harmonic degrees 1 to 6. Nevertheless the main features of these two observed patterns are present in the computed maps, and 4 out of 6 correlation coefficients lie close to the 90% confidence level. This is true for the geoid as well as for the surface divergence of the displacement velocity. However, as the internal viscosity structure has been assumed to have spherical symmetry, the rotational component of the surface velocities cannot be predicted.

Introduction

The geoid is an equipotential surface of the Earth's gravitational field which practically coincides with the mean surface of the oceans. Its deviation from an ellipsoidal shape reveals the existence of lateral density variations at all depths and scales. The most prominent undulations are at long wavelengths. At first sight, they exhibit no clear correlation with surface features: hence their great interest for theoretical geodynamics. The seismic tomography picture of the Earth's mantle which has emerged in recent years provides a new data set which can be used to understand mantle dynamics and its surface expressions, in particular gravity and plate velocities. A first level of physical understanding of these observables has now been established.

The distribution of seismic velocities reveals lateral variations of a few percent in the upper mantle [*Woodhouse and Dziewonski*, 1984; *Nataf et al.*, 1986; *Tanimoto* 1986] and about 1% in the lower mantle [*Dziewonski*, 1984]. The spatial resolution corresponds to spherical harmonic degree 6 or 8, i.e., at best to some 5000 km of lateral extent. Radially, the resolution varies from 100 km at shallow depths to more than 500 km near the core boundary. By assuming that these observed patterns reflect temperature fluctuations, one can identify low (high) density anomalies with regions of slow (fast) wave propagation. A first attempt to predict the shape of the geoid on the basis of these deep density structures alone led to a promising but puzzling result: the correlation between observed and computed geoid for the lower mantle sources was significant for degrees 2 and 3, but negative [*Dziewonski*, 1984]. No correlation was found for higher degrees or for upper mantle sources.

The negative sign of the predicted long wavelength geoid can be removed by considering dynamic mantle models with internal loading [*Ricard et al.*, 1984; *Richards and Hager*, 1984; *Lago and Rabinowicz*, 1984]. The internal loads induce a circulation which deflects the existing density interfaces such as the core-mantle boundary and the outer surface. The amplitudes of these topographies are very sensitive to the assumed radial viscosity structure. They generate additional contributions to the gravity field, not all with the same sign. For a viscosity contrast between upper and lower mantle not larger than 30 the dynamically induced deflection at the Earth's surface yields the dominant term. Its sign is opposite to that of the deep source: hence the negative correlation between this deep density structure and the geoid. On the contrary, a stiffer lower mantle can sustain internal loads with more efficiency so that the induced surface deflection is much weaker. In this case, internal sources could indeed directly determine the sign of the geoid.

The relevance of dynamic Earth models predicting observables such as the geoid and the surface velocities strongly depends upon two ingredients. Firstly, the capability of the physi-

Paper number 89JB00960
0148-0227/89/89JB-00960$05.00

cal model to reflect mantle processes realistically. This will be discussed later. Secondly, the quality of the data defining the internal loads. This raises the question of the validity of the tomographic data, and of the choice to make when several sets are available. For the lower mantle, we had no choice as only one model is published, even though another one [*Clayton and Comer*, 1983] has already been used for the same purpose [*Hager et al.*, 1985]. For the upper mantle the three models available include one [*Tanimoto*, 1986] which is preferred by some authors [*Richards and Hager*, 1986] but not by us because it ignores crustal corrections and shows little correlation at shallow depths with structures like oceanic ridges or cratons. The other two models [*Nataf et al.*, 1986; *Woodhouse and Dziewonski*, 1984] detect these expected warm or cold tectonic provinces. They contain other common features, for example, under the Red Sea or Central Pacific areas. Lately the model by Woodhouse and Dziewonski has been confirmed by the analysis of an even larger set of seismic data [*Dziewonski and Woodhouse*, 1988]. This determined our selection.

The uncertainty of the tomographic models becomes larger at higher harmonic degrees. On the other hand the lower degrees are enhanced when the geoid is computed. The most prominent features of the geoid are thus not very sensitive to uncertainties of the tomography at high degrees. Additionally one should remember that the power spectrum of the observed geoid starts at $l = 2$ and strongly falls as l increases.

The prediction of the geoid components of degrees $l = 2$ and 3 on the basis of lower mantle tomography alone is best for an Earth model where the mantle viscosity increase at 650 km is not larger than 10 [*Hager and Richards*, 1984; *Ricard et al.*, 1985; *Hager et al.*, 1985]. Such a small viscosity contrast between upper and lower mantle agrees with the conclusions of post-glacial rebound [*Wu and Peltier*, 1982] and Chandler wobble studies [*Yuen et al.*, 1982]. The predicted amplitude of the geoid is also satisfactory when the assumed proportionality between seismic velocity v_p and density ρ falls within the range of experimental values ($\partial v_p/\partial \rho$ = 3-4 km s^{-1} / g cm^{-3}). The above results imply a 650 km discontinuity which can be penetrated by the induced flow. This means that this interface between upper and lower mantle is purely physical. In models where this interface marks an intrinsic density step, the flows above and below are separated but coupled. One then speaks of a chemical boundary. Such models are not quite as successful in matching the geoid amplitude with the low degree mass heterogeneities of the lower mantle [*Hager et al.*, 1985].

For the upper mantle the tomographic model is given in terms of Δv_s^2 [*Woodhouse and Dziewonski*, 1984]. We simply assume that $\Delta v_s^2 = 2 v_s \Delta v_s$, where v_s is taken from the Preliminary reference earth model (PREM) [*Dziewonski and Anderson*, 1981] and varies with depth. The importance of density heterogeneities in the upper mantle thus depends upon the value of $\partial v_s/\partial \rho$. The poor correlation with the geoid suggests that the velocity distribution above 650 km could be linked to both temperature and chemistry fluctuations. However one specific correlation is noticeable: the long wavelength geoid is always high over subduction zones. Unfortunately, global tomography is not yet capable of detecting the subducting slabs. Their excess mass characterized by a parameter $L \Delta\rho$, where L is the lithospheric thickness, can be inserted in dynamic Earth models to compute a geoid. The result is particularly well correlated with observations for degrees $l = 4$ to $l = 9$, if one assumes a very large viscosity contrast at 650 km, say more than 100 [*Hager*, 1984]. As this stiff lower mantle is capable of supporting the weight of the dipping slabs, the induced surface depression is negligible and the gravity signal has the sign of the excess density of the slab. This result however contradicts the conclusion of a rather uniform mantle viscosity deduced from lower mantle loading.

The tomography data set has recently been used in conjunction with dynamic Earth models in order to predict not just the geoid but also the surface velocities [*Forte and Peltier*, 1987]. The latter can be compared with known plate velocities. This new approach has the advantage of being sensitive to the absolute value of mantle viscosity. It yields a satisfactory pattern for the divergence of the surface velocity field near oceanic ridges. The convergence zones however cannot be correctly predicted, most likely because of the lack of tomography signal associated with the subducting oceanic slabs. The required viscosities (2×10^{21} Pa s in the upper mantle) are close to those derived from post-glacial rebound and the increase within the lower mantle is not more than one order of magnitude. An additional test could easily be performed by including the contribution of the slabs to the total internal loads. These slabs are indeed known to be of prime importance for plate dynamics [*Forsyth and Uyeda*, 1975; *Richardson et al.*, 1979].

All Earth models described above, as well as those which will be found in the present paper, have one major limitation: they assume a purely radial viscosity structure, i.e., they forbid the very existence of lithospheric plates with their weak boundaries. The predicted surface velocity field is therefore purely poloidal, i.e., without any shear or toroidal component. For the real Earth both components are equally excited [*Hager and O'Connell*, 1979]. Some first models including lateral viscosity variations inside the outermost shell of the Earth are now available [*Ricard et al.*, 1988]. They predict several features of the geoid such as the marked maxima over convergence zones, and weaker minima over the softer ridge structures. In the present paper, however, no attempt will be made to include similar departures from spherical symmetry in the viscosity distribution.

We shall perform a series of tests using our selection of available data for internal loads (tomography and slabs) and the present state-of-the-art dynamic Earth models with a purely radial viscosity distribution. In order to investigate as large a variety of viscosity values as possible, we have established a straightforward Monte Carlo inversion procedure. The predictions of each model are compared with the real geoid and plate velocity divergence for degrees between 1 and 6. The best fitting models out of some 60,000 are then selected and discussed. The Monte Carlo

approach was already introduced in geophysics in order to construct elastic Earth models satisfying seismic observations [*Press*, 1970].

Monte Carlo Selection

We use the tomography data set L02.56 for the lower mantle [*Dziewonski*, 1984]. It includes degrees l = 1 to 6. For the upper mantle we take the M84C set of data [*Woodhouse and Dziewonski*, 1984] truncated beyond l = 6. To this we add a file describing the density anomalies associated with the seismic portions of subducting slabs. This file was provided by B. Hager who made use of it for some of his own models [*Hager*, 1984].

To convert the above spatial distributions into densities we need the values of three parameters: L $\Delta\rho$, $\partial v_s/\partial\rho$, and $\partial v_p/\partial\rho$. The second derivative was proposed to amount to 3-4 km s^{-1} / g cm^{-3} by comparing the observed low degree geoid and that predicted by a model with internal loading restricted to the lower mantle [*Hager et al.*, 1985]. Experiments with the relevant oxides and silicates yield values of $\partial v_p/\partial\rho$ between 3 and 10 km s^{-1} / g cm^{-3} [*Sumino and Anderson*, 1984]. In our models, we allowed this derivative to vary from 1 to 13 km s^{-1} / g cm^{-3}. The same laboratory measurements indicate a value around 3 km s^{-1} / g cm^{-3} for $\partial v_s/\partial\rho$. In order to allow for a possible chemical rather than thermal origin of the velocity variations in the upper mantle, we let this parameter vary from 1 to 80 km s^{-1} / g cm^{-3}. The large value of the upper bound tends to damp the density fluctuations, i.e., to attribute the observed seismic pattern to a possible petrological distribution without associated density changes.

The free parameter L $\Delta\rho$ for the slabs can be estimated by comparing the bathymetry of ridges to that of old ocean floors. Isostasy requires L $\Delta\rho$ to be equal to the increase in water depth, say 4 km, times the density difference between mantle rocks and water, say 2300 kg m^{-3}. In our dynamic Earth models we therefore allowed the value of L $\Delta\rho$ to vary between 3.0×10^6 and 1.5×10^7 kg m^{-2}. The lower bound corresponds to a situation where the added slabs have a small density contrast and are not essential in the model. This could also be interpreted as an indication that their signature is already present in the tomography signal. The upper bound, on the contrary, would suggest that the dense slab structure could extend beyond the seismicity limit, as suggested by wave propagation analysis [*Creager and Jordan*, 1984]. Another possible parametrization would thus consist in varying the length of slabs rather than their density [*Hager*, 1984]. This alternative is not equivalent to the choice made in this paper, in the sense that the Green function relating the loads to the induced geoid can change markedly with depth. The density differences represented by the subducting slabs are certainly of large magnitude, but very localized. Therefore their amplitude content at degrees 2 to 6 of spherical harmonics is indeed rather weak in comparison with the density heterogeneities defined by upper mantle tomography. For $\partial v_s/\partial\rho$ = 5 km s^{-1} / g cm^{-3} and a slab thickness L = 100 km, seismic tomography yields density fluctuations of amplitude 0.05 g cm^{-3} at 300 km depth, whereas the additional contribution derived from the existing slab configuration amounts to 0.08 g cm^{-3}.

For a given internal density distribution, the geoid N and surface divergence $\vec{\nabla}.\vec{v}$ of the induced flow can be computed for any chosen viscosity profile within the sublithospheric mantle. Here we assume a reference viscosity η_0 in the upper 100 km, and divide the remaining mantle in three layers with interfaces at depths of 300, 650 and 2900 km, and with viscosities η_1, η_2, and η_3, respectively. These viscosities are allowed to scan several decades: η_1 can vary between η_0 and $10^{-4}\ \eta_0$, η_2 has a broader range from $10^3\ \eta_0$ to $10^{-4}\ \eta_0$, while in the lower mantle η_3 can take values between 10 η_0 and $10^{-3}\ \eta_0$. Both physical and chemical interfaces at 650 km have been considered, depending upon the possibility for the induced flow to cross this boundary. The general formalism is fully described in recent papers [*Ricard et al.*, 1984; *Richards and Hager*, 1984; *Forte and Peltier*, 1987] and consists in computing Green excitation functions for each spherical harmonic degree. A convolution of the Green function with the radial load distribution is then carried out for every degree l and order m. This yields the computed coefficients ${}^cN_{lm}$ for the geoid and ${}^c(\vec{\nabla}.\vec{v})_{lm}$ for the surface velocity divergence.

Each dynamical model we computed includes six free parameters: L $\Delta\rho$, $\partial v_s/\partial\rho$, $\partial v_p/\partial\rho$, η_1/η_0, η_2/η_0, and η_3/η_0. As our expansion in spherical harmonics is limited to degree 6, a given model predicts 45 geoid coefficients (degrees 2 to 6) and 48 velocity divergence coefficients (degrees l = 1 to 6). Notice that the viscosity η_0 of the outermost layer has a prescribed reference value. The value of the geoid reflects the force equilibrium between applied loads and induced interface deflections. It is sensitive to the viscosity structure, but not to the absolute value of the viscosity. On the contrary, the absolute amplitude of $\vec{\nabla}.\vec{v}$ is proportional to the ratio of source load intensity and absolute value of the viscosity. If one restricts the comparison between modeled and observed velocities to the individual correlation coefficients one can only determine viscosity ratios for the structure as well as density ratios for the loads. Our procedure is restricted to relative velocity values in order to avoid the difficulties associated with the unsolved problem of the equipartition of energy between poloidal and toroidal fields.

For a given model the above six free parameters are chosen within each of the allocated ranges of values. Two selection criteria are then calculated in order to determine the best possible models. It is usual to consider the correlation coefficients between computed models and observations for each degree. However, a good correlation at all degrees does not imply a satisfactory prediction of the amplitudes or of the global shape. On the other hand, the confidence level of a global correlation including all degrees together is only meaningful when the coefficients of the spherical harmonics do not decrease too sharply in amplitude as l increases. This last condition holds for the velocity divergence $\vec{\nabla}.\vec{v}$, but does not apply to the geoid N

[*Kaula*, 1966]. One thus defines two different selection criteria:

$$C_v = \frac{\sum_{l,m}^{\leq 6} {}^c(\vec{\nabla}.\vec{v})_{lm} \, {}^o(\vec{\nabla}.\vec{v})_{lm}}{\sqrt{\sum_{l,m}^{\leq 6} {}^c(\vec{\nabla}.\vec{v})^2_{lm} \sum_{l,m}^{\leq 6} {}^o(\vec{\nabla}.\vec{v})^2_{lm}}} \quad (1)$$

$$C_N = \frac{1}{4\pi} \left(\sum_{l,m}^{\leq 6} \left({}^cN^2_{lm} + {}^oN^2_{lm} - 2 \frac{\sum_{m}^{\leq 1} {}^c(\vec{\nabla}.\vec{N})_{lm} \, {}^o(\vec{\nabla}.\vec{N})_{lm}}{\sqrt{\sum_{m}^{\leq 1} {}^c(\vec{\nabla}.\vec{N})^2_{lm} \sum_{m}^{\leq 1} {}^o(\vec{\nabla}.\vec{N})^2_{lm}}} \right) \right)^{1/2} \quad (2)$$

Here the upper index o refers to observations, as c stands for computed values. The first criterium C_v corresponds to the correlation coefficient for $\vec{\nabla}.\vec{v}$. It includes all degrees from $l = 1$ to 6. A good model yields a maximum value of C_v, close to unity. The second criterium C_N expresses the root mean square difference between observed and predicted geoid. This residual variance is given in meters, and can thus be compared with the average amplitude of the total geoid when degrees $l = 2$ to $l = 6$ are taken into consideration, which amounts to 41 m. A good model should minimize the misfit given by the value of C_N. By inspection of the above formula one sees that a minimum C_N requires maximum values for all correlation coefficients calculated for each degree as well as globally for all degrees. Quantitatively the value of C_N is obviously dominated by the largest coefficients, i.e., those of degrees 2 and 3 which have average amplitudes of 33.7 and 19.2 m. For degrees 4, 5 and 6, this amplitude drops to 10.0, 7.6 and 5.5 m.

Models With Internal Loading

In this section we mainly examine the results of the selection procedure based on the best fit to the geoid, according to criterium C_N. In order to reduce computing time we usually ran some 3000 models with random values of the six free parameters described above. The allowed values in this random selection are regularly distributed on a logarithmic scale for the viscosities and on a linear scale for the densities. For each parameter the allowed range was then cautiously reduced around the group of values corresponding to the best 100 solutions. A new set of 3000 models was then tested. This procedure was repeated six times and satisfactory convergence was achieved. The first steps of the Monte Carlo selection revealed the existence of two classes of solutions for the mantle viscosity structure. For class 1 the viscosity stratification implies changes by less than two orders of magnitude. For class 2 a strikingly stiff layer is found at the bottom of the upper mantle, with a viscosity contrast of order 10^4. For clarity these two types of solutions will be presented separately.

Class 1 Solutions: Geoid

Figures 1 and 2 each depict the 15 best sets of free parameters selected for a mantle having either a physical or a chemical interface at 650 km depth. For class 1 the viscosity between 300 and 650 km is not allowed to take values much in excess of that of the 100 km thick lithosphere. In both cases the fit is somewhat satisfactory, as C_N amounts to 31 m. Thus 24% of the real geoid up to degree 6 is explained by the best models. By comparison the best two-layer model of *Forte and Peltier* [1987] yields a mean discrepancy C_N of 33 m for degrees up to 5 only, and a weaker viscosity contrast. Here the selected viscosity structure of Figure 1 singles out the presence of a stiff lithosphere with a reference viscosity η_0 and exhibits a marked jump by a factor of 50 between upper and lower mantle. In Figure 2, i.e., in the presence of a chemical boundary at 650 km, the structure is more homogeneous, except for a narrow asthenospheric channel. The upper histograms in both figures show that the density of the slabs is not well resolved by the models. In Figure 1, the partial derivatives of the seismic velocities are on the contrary well defined, as seen in the middle and lower histograms. The preferred values of $\partial v_s/\partial\rho$ are well within the range of experimental results and thus seem to rule out a predominantly petrological explanation for the observed distribution of seismic velocities in the upper mantle. For the lower mantle our preferred value of $\partial v_p/\partial\rho$ is higher by 50% than that found by previous authors [*Hager et al.*, 1985] and remains compatible with experimental values [*Sumino and Anderson*, 1984]. In Figure 2, the middle histogram still favors a thermal rather than a petrological origin for the upper mantle heterogeneities. The low value of $\partial v_p/\partial\rho$ in the lower histogram points to the presence of density heterogeneities of large amplitude in the lower mantle.

It is customary to plot the correlation coefficients between predicted and observed spherical harmonic coefficients degree by degree. This is done in Figure 3 for the geoid. The squares correspond to the best solution among the 15 given in Figure 1 for a physical interface. For this solution the 6 parameters take the values 0.003, 0.0035, and 0.25 for the three viscosity ratios, and 9.6×10^6 kg m^{-2}, 5.0 km s^{-1} / g cm^{-3}, and 6.0 km s^{-1} / g cm^{-3} for the density coefficients. Notice that for $l = 2$, 3, 4, and 5 the coefficients lie close to or above the line of 90% confidence level. This statement alone could be misleading, because as mentioned above this best solution explains only 24% of the geoid mean amplitude. This illustrates the general remarks we made before defining C_v and C_N: a good correlation between orders is certainly required, but the amplitudes for all degrees must also coincide. This last aim is not quite reached yet. In the same figure the circles correspond to the best solution included in Figure 2 for a chemical interface. Here the 6 parameters amount to 0.01, 0.32, 0.28, 12.6×10^6,

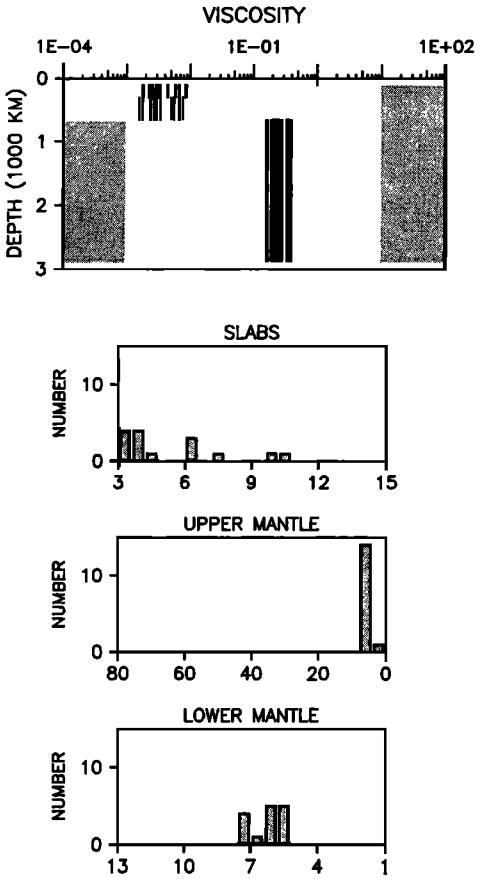

Fig. 1. Set of six free parameter values corresponding to the 15 best solutions selected by a Monte Carlo method. The model Earth has a 100 km thick lithosphere with viscosity $\eta_0 = 1$, and 3 layers with unknown viscosities. The circulation induced by internal loads is allowed to cross the 650 km interface between upper and lower mantle: this sort of interface is called physical. Each solution yields a computed geoid which has been compared with the observed one by means of (2). The upper diagram depicts the selected viscosity profiles within a prescribed range limited by the shaded domains proper to class 1 solutions. Below this, 3 histograms describe the distribution of the best values for density parameters. The upper one gives the number of solutions versus the value of the slab parameter L $\Delta\rho$ expressed in 10^6 kg m^{-2}. This parameter is not well constrained. Similarly the middle histogram is for upper mantle heterogeneities: the horizontal axis give the allowed values of $\partial v_s/\partial\rho$ inkm s^{-1}/ g cm^{-3}. Notice that 14 solutions out of 15 happen to have the same value for this parameter. Finally the lower histogram is drawn relative to $\partial v_p/\partial\rho$ for the lower mantle. The best solutions are grouped around 6 km s^{-1}/ g cm^{-3}. The orientation of the abscissae for each histogram is such that a selected parameter value located on the left hand side corresponds to a smaller amplitude of the density anomaly than one located on the right hand side. For oceanic slabs the most probable value of L $\Delta\rho$ lies in the middle portion of the horizontal axis. Experimental values of the derivatives of seismic velocities versus density also lie in the middle portion of the horizontal axis of the lower histogram, but are at the extreme right for the middle one.

1.6, and 2.0 with the same units as above. Notice that although these correlation coefficients are different from the previous ones, this solution also explains a sizable portion (24%) of the ob-

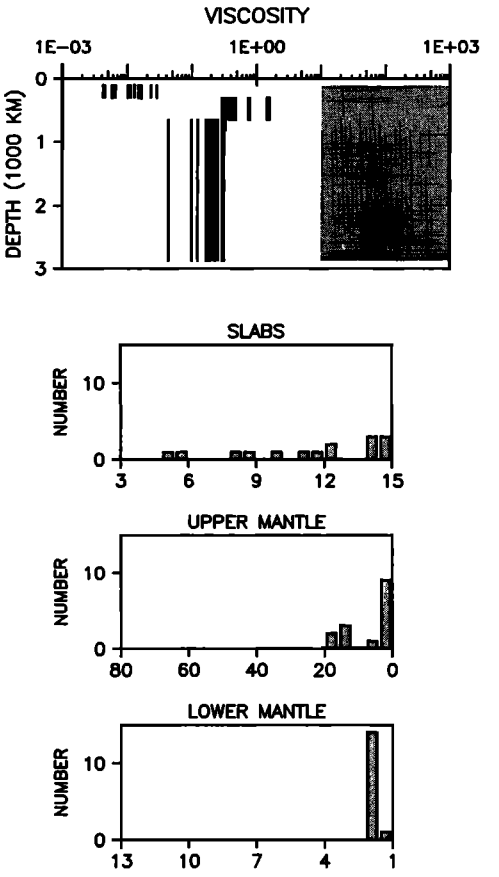

Fig. 2. Same as Figure 1, but for model Earth structures with a chemical interface at 650 km, i.e., in which the circulation is not allowed to cross that boundary . Notice that the low viscosity is only present in the upper part of the upper mantle. The lower histogram points to a strong contribution from lower mantle heterogeneities.

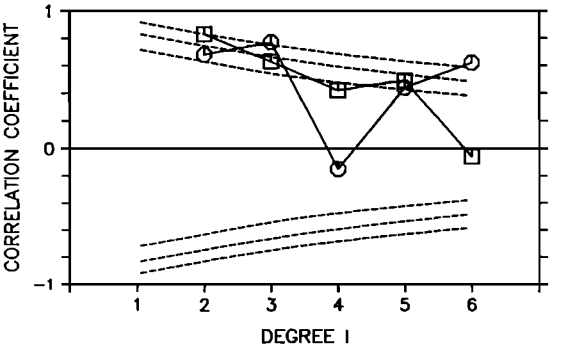

Fig. 3. Correlation coefficients for spherical harmonic degrees 2 to 6 between computed and observed geoid for the best solution without (squares) or with (circles) a chemical interface at 650 km. The three pairs of dashed curves indicate confidence levels of 80, 90 and 95%, respectively.

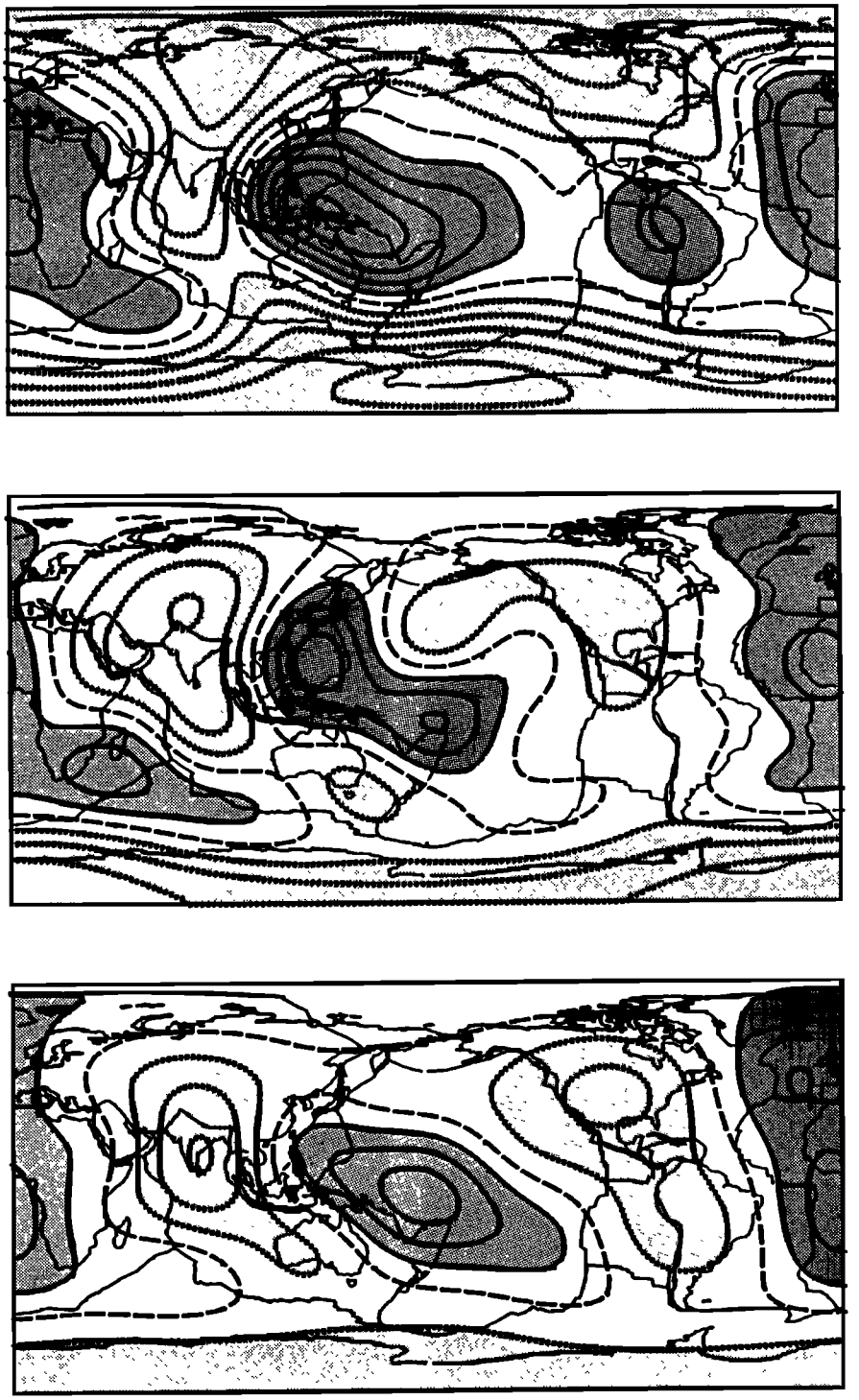

Fig. 4. Observed (top map) and predicted (lower maps) geoids for spherical harmonic degrees 2 to 6. The level lines are 20 m apart and the regions above 20 m or below -20 m are heavily or lightly shaded. The middle map derives from our best class 1 solution with a physical interface at 650 km. It thus corresponds to one of the set of six parameters included in Figure 1 and to the correlation coefficients of Figure 3 (squares). The lower map corresponds to the best solution with a chemical interface at 650 km, and is similarly related to Figures 2 and 3 (circles).

served geoid. If one computes the three separate contributions from slabs, upper mantle and lower mantle one finds that the last one is largely dominant. This is not true for the model including a physical interface: in that case the lower and upper mantle sources are equally important, but the slab contribution is still negligeable.

The hydrostatic geoid truncated above degree 6 is plotted at the top of Figure 4 and compared with our best two predicted solutions. The middle

and lower maps depict the computed geoids for a mantle with physical or chemical interface at 650 km. They thus correspond to the two sets of correlation coefficients of Figure 3. Visually, the main equatorial maxima over Africa and western Pacific are well predicted, as is the trough of minimum amplitude over India. The main shortcomings are in the insufficient polar flattening and in the absence of a maximum over South America.

Class 2 Solutions: Geoid

These solutions were isolated from those depicted in the above section by imposing a lower bound to the possible values of the viscosity between 300 and 650 km. This lower bound is identical with the upper bound imposed to the class 1 solutions. Figure 5 depicts the new best 15 sets of selected parameters for a physical interface at 650 km. The most striking feature is a very stiff bottom layer for the upper mantle. It damps the flow velocities at this level. There is thus not much difference in dynamical behavior with a model mantle having a chemical interface and the same stiff layer. These last solutions were also found, and are indeed quite similar, as seen in Figure 6. The other remarkable feature depicted by the histograms of Figures 5 and 6 is the good definition and high value for slab densities, the

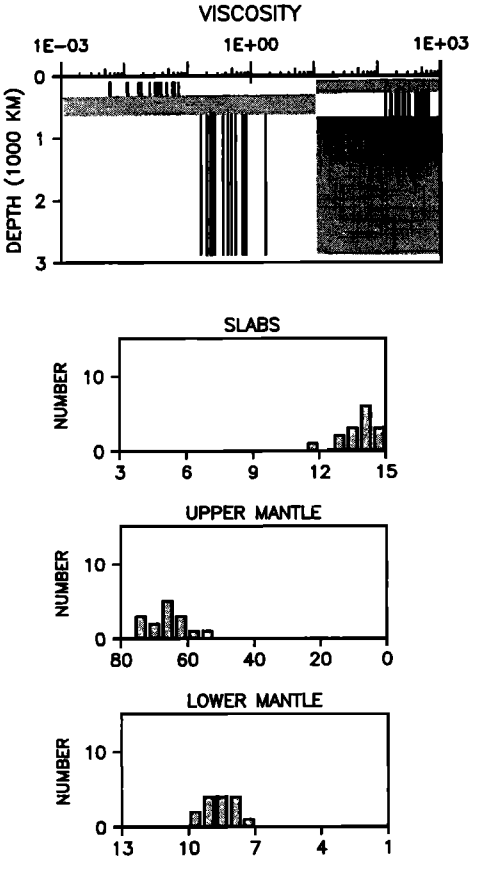

Fig. 5. Same as Figure 1, but for the 15 best class 2 solutions. For this class the shaded area shows that the bottom of the upper mantle is allowed to exhibit high viscosity values. Here the selected density parameters in the histograms show that the preferred solutions imply very dense subducting slabs.

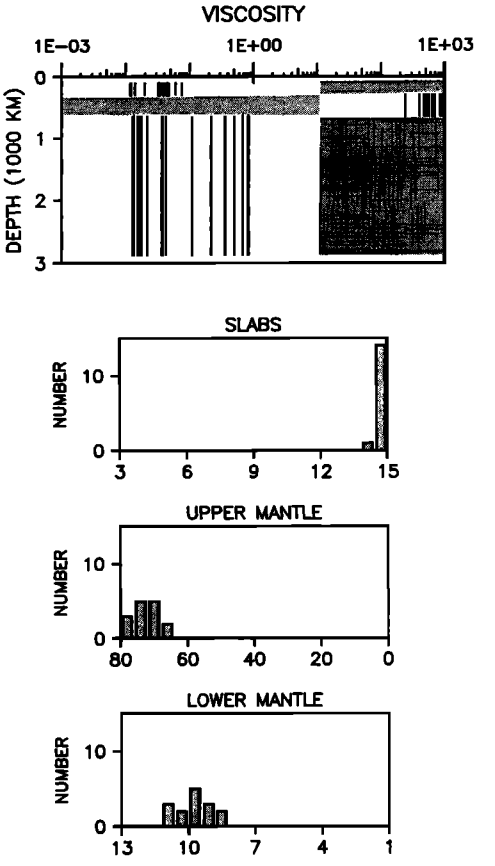

Fig. 6. Same as Figure 2 but for the 15 best class 2 solutions. As in the case of a physical interface (Figure 5) the slabs are dense with a very well defined distribution.

vanishing amplitudes of the other density heterogeneities in the upper mantle and the rather weak heterogeneities in the lower mantle. The best two solutions among those shown in the last figures correspond to a residual geoid of 28 m in both cases. Therefore it explains 32% of the observed geoid. The six free parameters amount to 0.018 (respectively 0.039), 260 (875) and 0.83 (0.82) for the viscosities, and 15×10^6 (respectively 15×10^6) kg m^{-2}, 67 (70) km s^{-1} / g cm^{-3}, and 8.2 (9.7) km s^{-1} / g cm^{-3} for the densities. The correlation coefficients between observed and computed quantities are given on Figure 7. By comparison with Figure 3 one notices that the class 2 solutions give a better fit than those of class 1, as can also be appreciated from the already mentionned values of C_N (misfit of 28 instead of 31 meters). Figure 8 maps the predicted geoid for these best class 2 solutions. They are very similar. By comparison with the class 1 solutions of Figure 4 one notices a slight improvement over South America and the persisting weakness of the polar flattening.

Predicted Surface Velocities

We now turn to the problem of constructing dynamical Earth models with the same internal loads as above, but with the purpose of predicting the observed velocity divergence of plate tectonics. The same Monte Carlo tests were performed on the

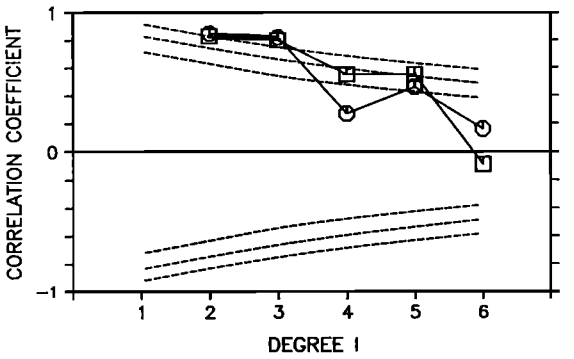

Fig. 7. Same correlation coefficients as in Figure 3, but for both best class 2 solutions. Squares are again for a model Earth with a physical interface at 650 km, and circles for a chemical interface.

basis of maximizing the correlation criterium C_v defined earlier. As we do not solve for the absolute values of the velocities, but for relative variations, we have fixed a scaling factor for the loads by taking $L\,\Delta\rho = 10^7$ kg m^{-2}. As already noticed by *Forte and Peltier* [1987] the predicted surface velocities are not very sensitive to the relative radial variations of the viscosity. Both best solutions for a physical or chemical interface at 650 km tend however to exhibit a stiff layer at the botom of the upper mantle, as was the case in class 2 solutions for the geoid. Moreover these solutions lead to high values of the two derivatives related to upper and lower mantle densities. This means that the role of the slabs is enhanced with respect to that of density heterogeneities derived from seismic tomography. Our best solutions yield a value of 0.82 for C_v. Taking account of the 48 harmonic coefficients involved here, this means that with an adequate value of the reference viscosity η_0, 82% of the observed root mean square plate velocity divergence is predicted by our best models. This corresponds to a statistical confidence level larger than 99,9%.

As the inversion for the velocity turns out to have less resolving power for the mantle viscosity distribution than that obtained by fitting the geoid, we now turn to a different approach. It consists in computing the surface velocity divergence for the solutions used to predict the best geoids of class 1 and 2. In Figure 9 the top map depicts the observed velocity divergence for

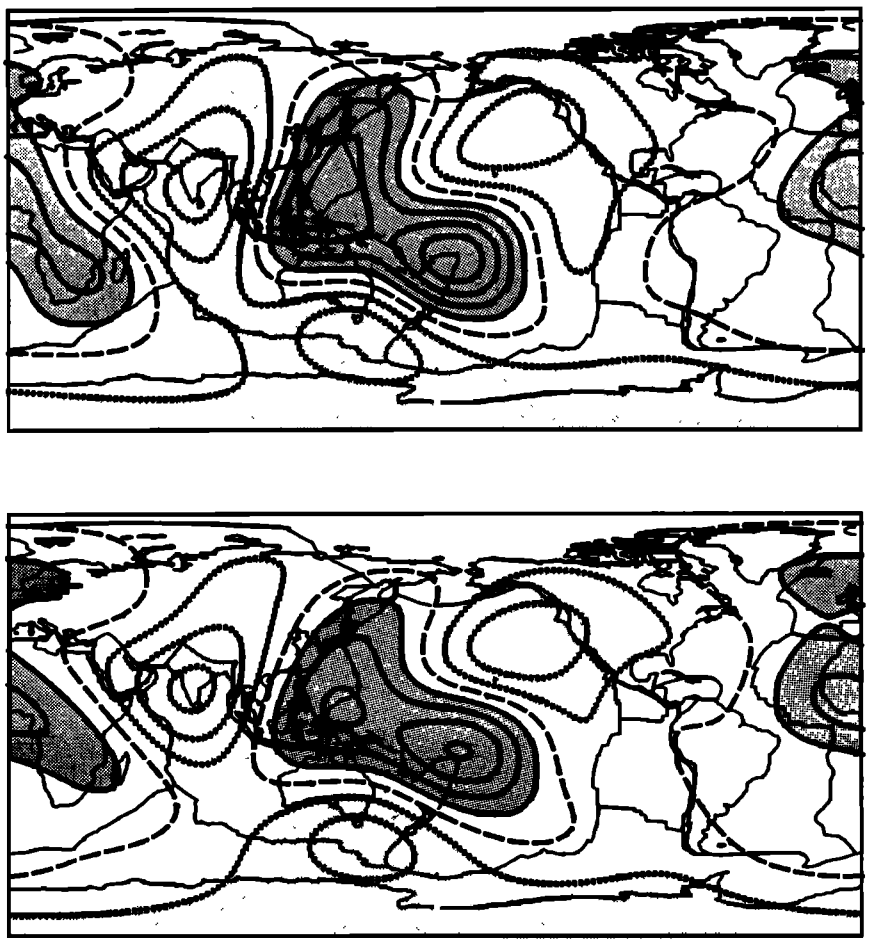

Fig. 8. Maps of the predicted geoid corresponding to the best class 2 solutions. The top map is for an Earth model with physical interface at 650 km; the lower one for a chemical interface at the same depth. These maps can be compared to those of Figure 4, in particular to the top one corresponding to the observed geoid. The spacing between level lines is again 20 m.

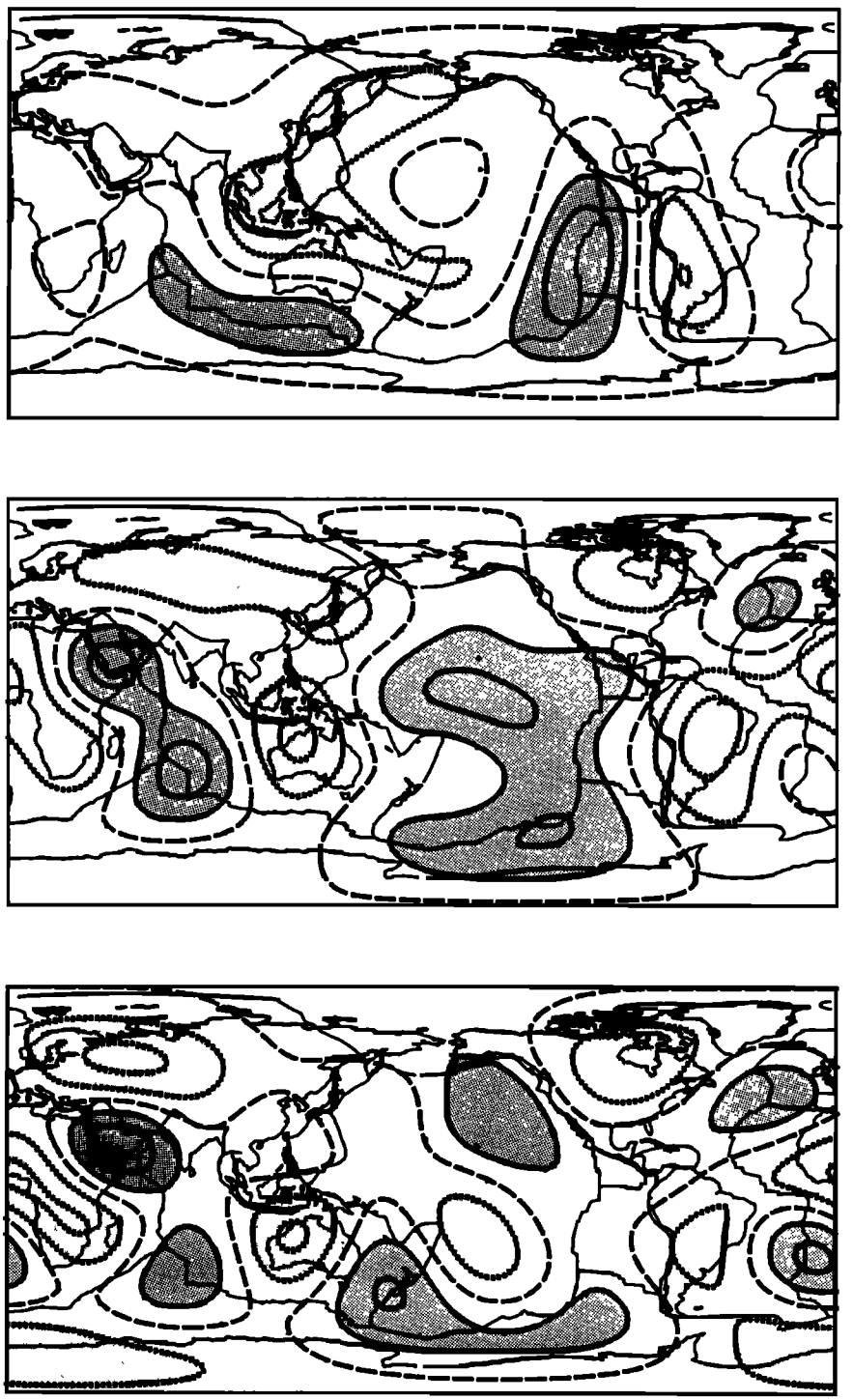

Fig. 9. Divergence of surface displacement velocities for spherical harmonic degrees 1 to 6. The top map corresponds to observed plate velocities with marked maxima over oceanic ridges (heavy shading) and minima over subduction zones (light shading). The other two maps depict predicted values for our best class 1 solutions. Each map is normalized and has 5 level lines. The middle one gives the velocity divergence predicted on the basis of the solution used to plot the middle geoid in Figure 4. It accounts for 44% of the observed velocity pattern. The lower one only accounts for 26% of the observations. It derives from the best solution with chemical interface as did the lower geoid map in Figure 4.

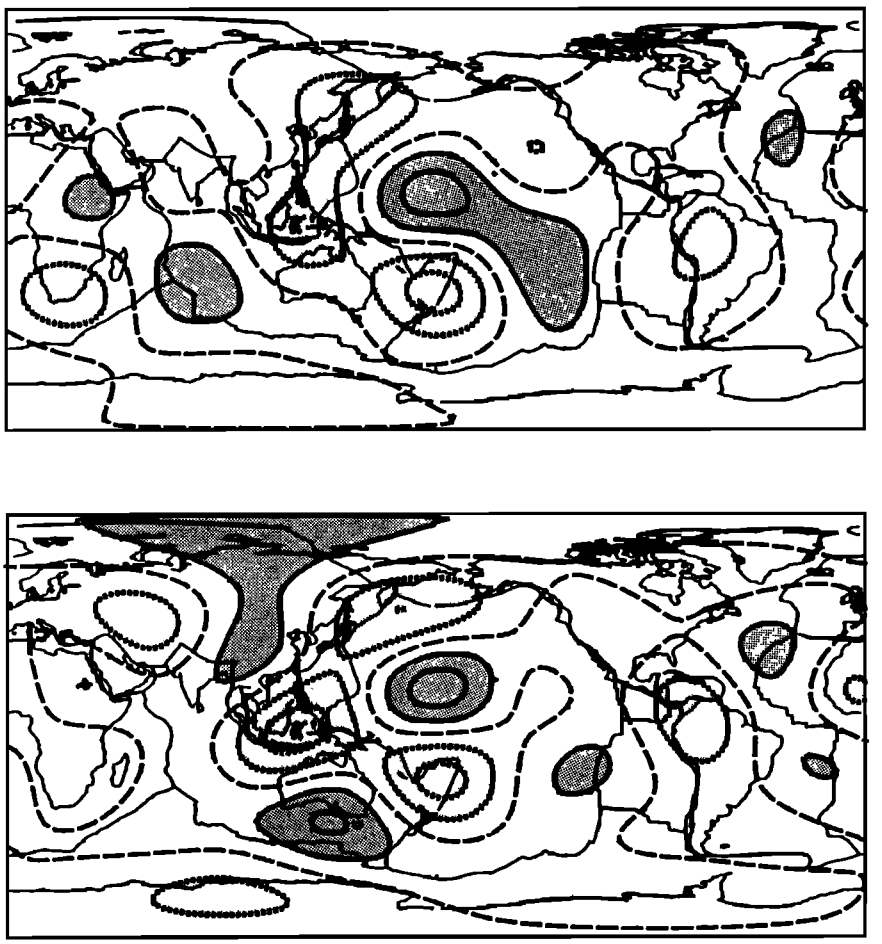

Fig. 10. Same as Figure 9 but for our two best class 2 solutions, i.e., either with (top) or without (bottom) chemical interface at 650 km. They respectively account for 56% and 64% of the observed pattern depicted at the top of Figure 9. In the lower map, the spurious zone of opening along about 90° longitude has a size which is exaggerated by the cylindrical projection. The convergence along the rim of the Pacific is well predicted as are the major oceanic zones of opening.

degrees l = 1 to 6. The middle and lower maps are predicted on the basis of the best solutions of class 1, first with a physical and second with a chemical interface. They correspond to geoids depicted in Figure 4. Our middle map is very similar to the preferred model of *Forte and Peltier* [1987] based on a two-layer mantle, and accounts for 44% of the observed pattern. This resemblance can be explained by two reasons: (1) the weak sensitivity of the Green functions of $\vec{\nabla}.\vec{v}$ to the radial viscosity variation, and (2) the absence or relative weakness of the internal loads corresponding to oceanic slabs in both investigations. The lower map only accounts for 26% of the observations. Notice that the computed maps have the correct localization for the zones of opening corresponding to oceanic ridges. However they locate the zones of convergence beneath old dense cratons like Africa, South America, Australia, North America and Siberia.

Figure 10 corresponds to the best class 2 solutions already used to draw the predicted geoids in Figure 8. These velocity divergence maps predict 56%, respectively 64%, of the real pattern, a remarkable improvement. A comparison with Figure 9, which depicted the class 1 solutions, illustrates this point: convergence in the Western Pacific region has advantageously replaced the spurious downwelling of old cratons. This is of course not a surprise as the main driving force has been shifted to the slabs (see upper histograms in Figures 5 and 6). Figure 11 depicts the correlation coefficients for the velocity divergence corresponding to the above class 1 and class 2 solutions.

Models With Both Internal Loading And Imposed Surface Kinematics

The previous section showed that it is quite difficult to propose dynamic Earth models which satisfactorily predict both the geoid and the divergence of plate velocities. In particular, the relative importance of slabs and other mantle heterogeneities is not always the same for both criteria. Generally speaking the prediction of the velocity divergence has been more successful than that of the geoid. Now we shall consider the possibility of taking observed surface velocities in addition to internal loads as given contraints to compute the induced mantle dynamics and the associated geoid. Plate tectonics velocities con-

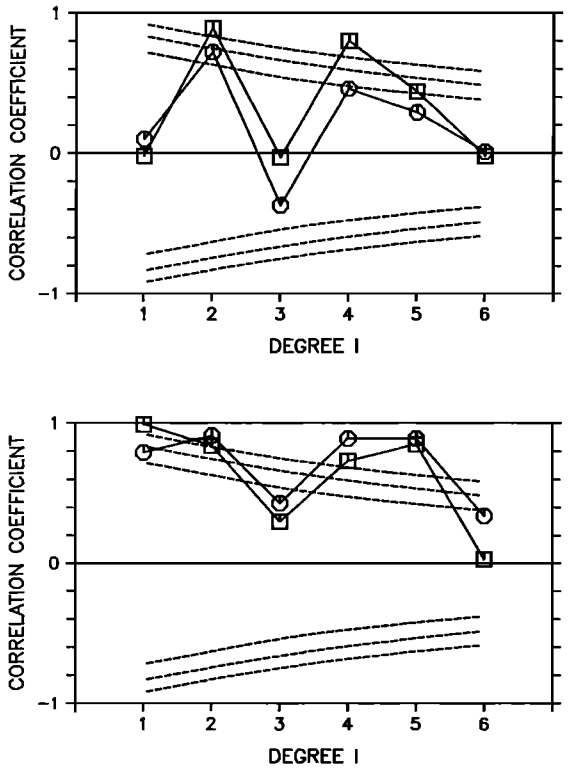

Fig. 11. Correlation coefficients between predicted and observed surface velocity divergence for degrees 1 to 6. The squares correspond to Earth models with physical interface at 650 km, whereas the circles are for the chemical interface at the same depth. The top graph applies to our best class 1 solutions which already yielded the correlation coefficients for the geoid given in Figure 3. The dashed curves define again the confidence levels 80, 90 and 95%. Similarly the lower graph applies to our best class 2 solutions, which also yielded Figure 7 for the geoid.

stitute a more robust set of input data than the emerging tomography picture. Their introduction in models with spherical symmetry for the rheological properties tends to simulate the rigidity of the lithosphere and the existence of localized plate boundaries. If the models described in the preceding section had been completely successful in their velocity predictions, the present procedure would of course not change the solutions.

The mathematical approach consists in superposing two subsolutions. The first one is excited by the internal loads as in the previous section, but a no-slip condition is imposed on the outer spherical surface of the model Earth which has no lithosphere. The second one is without internal loading and is excited by the observed horizontal velocity $\vec{v}$ restricted to harmonic degrees up to 6 and by a vertical flow component $L\,\vec{\nabla}.\vec{v}$, where L is again the lithospheric thickness. For the real Earth this velocity field corresponds to the surface velocities of the rigid plates and to downwelling or upwelling motion at plate boundaries. The resulting geoid is then compared with observations and the above criterium C_N is again minimized through a Monte Carlo trial. Each tested model now corresponds to absolute values of the viscosities, η_1, η_2, and η_3, and of the density parameters L $\Delta\rho$, $\partial v_s/\partial\rho$, and $\partial v_p/\partial\rho$.

Figure 12 shows the 15 best viscosity values and density parameters for a dynamic Earth with a physical interface at 650 km, excited by internal loads, and fitting observed surface velocities. The quality of the fit between computed and observed geoid is again improved: the mean discrepancy C_N is now 27 m, so that 34% of the geoid is predicted. The contrast in viscosity at 650 km is still two orders of magnitude, with an unexpected viscosity drop with depth in the upper mantle. However the average viscosity of the upper mantle is only twenty times lower than that of the deep mantle. The histograms in the lower part of the figure show poorly constrained and rather weak slab and upper mantle density anomalies. As far as the lower mantle is concerned the preferred density parameters are grouped around 6.5 km s^{-1} / g cm^{-3} as was the case in Figure 1.

The geoid predicted on the basis of the best solution contained in Figure 12 is depicted in Figure 13. For this solution, the values of the 6 free parameters are 3.0, 0.18, and 43 $x10^{21}$ Pa s for absolute viscosities, $3.3x10^6$ kg m^{-2}, 70, and 5.8 km s^{-1} /g cm^{-3} for density coefficients. This

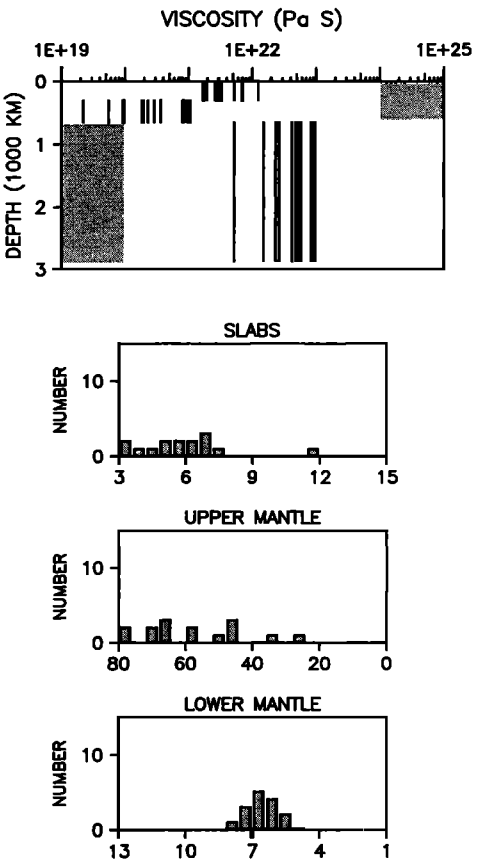

Fig. 12. Set of six free parameters yielding the 15 best geoids for dynamic models where both the internal loads and the surface displacement velocities are imposed. The 650 km boundary is physical, as in the case of Figure 1. The various diagrams are arranged as in Figure 1, but here the mantle viscosities are given in absolute values (Pa s). Notice also the absence of the lithosphere in these models, which only deal with the sublithospheric dynamics.

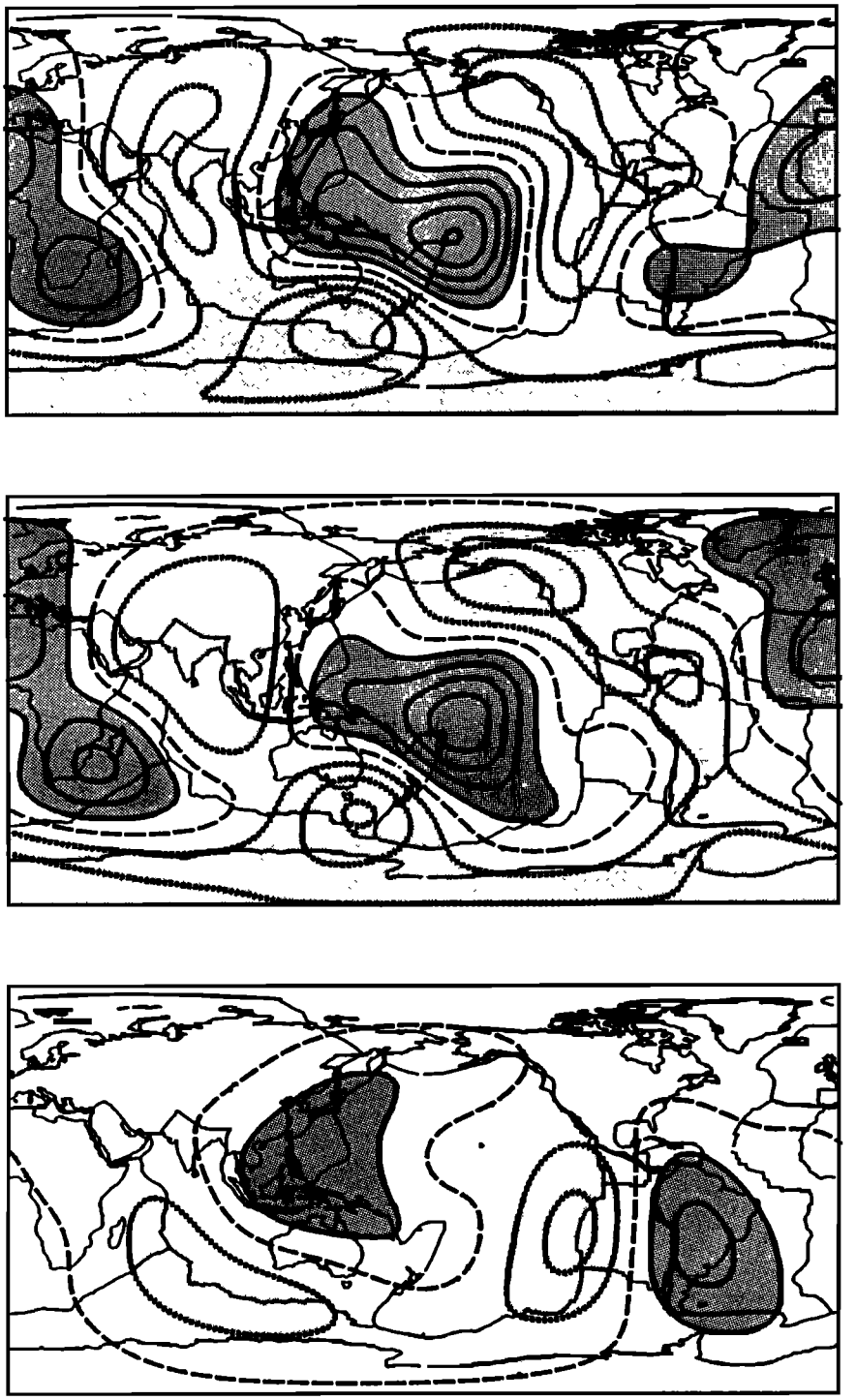

Fig. 13. Predicted geoid (top map) for the solution corresponding to the best set of parameters in Figure 12. The lower maps separately depict the contributions to this geoid from internal loading and imposed surface velocities. The latter have a vertical component beneath oceanic ridges and subduction zones. The level lines are again 20 m apart.

figure successively depicts the global solution and its 2 components derived with internal loads (middle map) or imposed surface velocities (lower map). The comparison with the real geoid found at the top of Figure 4 again shows a satisfactory correlation for the major highs and lows in equatorial regions, combined with a deficient polar flattening. Notice a real improvement over South America with a well defined local maximum. This is obviously caused by the kinematically induced component, as seen in the lower map. The latter also exhibits a marked minimum over the rapidly spreading East Pacific ridge, illustrating of course a clear anticorrelation with the map of

observed velocity divergence given at the top of Figure 9. Physically such a correlation can be understood because the plate motion drives a return flow with an associated positive horizontal pressure gradient between zones of opening and zones of convergence. The absence of strong minima over ridges in the real geoid could only derive from more elaborate models allowing for a weaker lithosphere under young oceans [*Ricard et al.*, 1988].

The observed velocity, combined with internal loads, has also been imposed on an Earth model with chemical interface at 650 km. Figures 14 and 15 depict the selected best values and the predicted geoid in the same manner as in both previous figures. The best solution yields the following parameters: 0.73, 9.4, and 520 $x10^{21}$ Pa s for the absolute viscosities and $11.2x10^{6}$ kg m^{-2}, 1.68, and 9.32 km s^{-1} / g cm^{-3} for the densities. The misfit C_N amounts to 28 m.

Figure 16 depicts the correlation coefficients degree by degree, for the above best Earth model with either a physical (top) or a chemical (bottom) interface. The solid squares are for the total predicted geoid, i.e., for the top maps of Figure 13 or 15. The confidence level is higher than 80% for most degrees. The circles and triangles denote the separate contributions to the predicted geoid by internal loading and imposed surface displacement velocities, respectively. These velocities play an important role for degrees 2, 4 and 5.

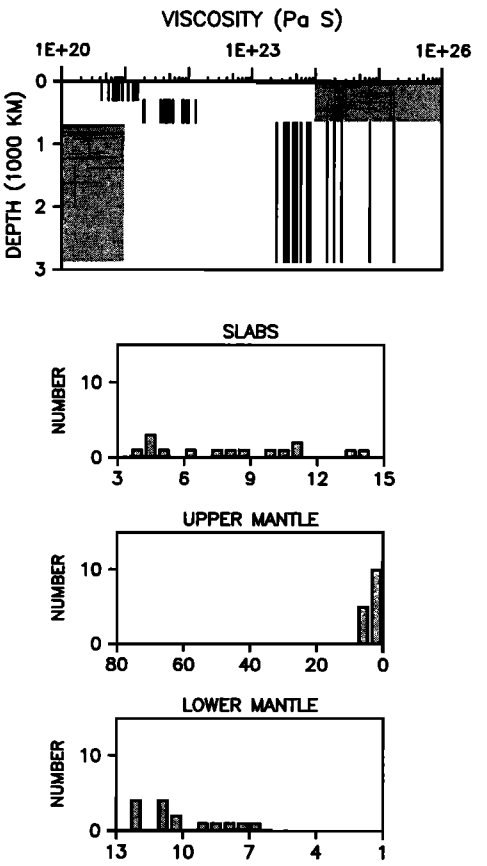

Fig. 14. Same results as in Figure 12 for an identical Earth model, with the exception that the 650 km depth interface is now chemical.

Conclusion

This work is based on the same rationale as earlier analyses published in the past 4 years. Its specificity lies both in the methodology and the scope. First, the Monte Carlo selection procedure with 6 free parameters represents a first attempt to treat the relationship between seismic tomography, plate motion and geoid as an inverse problem. Here the free parameters describe the mantle viscosity structure and the relative intensity of the density heterogeneities detected by seismic studies. A very large range of values of these physical quantities for dynamic Earth models has been investigated. The second specificity of this study is that three possible density sources in the mantle were included up to spherical harmonic degree 6, and that their relationship with both geoid and surface velocity field were considered simultaneously. The most complete studies up to now either neglected the tomography of the upper mantle and restricted themselves to degree 3 in the lower mantle [*Richards and Hager*, 1986], or neglected the dynamic contribution of slabs and were restricted to a two layer mantle [*Forte and Peltier*, 1987]. These earlier papers only explored a very limited range of parameter values for viscosity and density configurations.

Despite our effort to broaden the analysis, we remain aware of existing limitations. Seismology has only begun to unravel the three-dimensional structure of the Earth's interior. Other tomographic data sets than those used here are in existence [*Clayton and Comer*, 1983]. The assumed linear relationship between lateral variations in velocity and density may be oversimplified. In the same way the definition of dense slabs by the observed deep seismicity patterns may be too restrictive. Other limitations arise from the assumed spherical symmetry of the model viscosity structures, i.e., in particular from the difficulty to account correctly for the very existence of lithospheric plates with soft boundaries. However, one can claim a posteriori that many facets of global Earth dynamics are now beginning to be constrained by observations. Nevertheless various qualitative and quantitative conclusions reached here may call for revision in coming years.

The first lesson to draw from our Monte Carlo inversion derives from the inspection of Table 1, which summarizes the best performances of the computed models both for the geoid N and for the velocity divergence $\vec{\nabla}.\vec{v}$. Only 1/4 to 1/3 of the root mean square amplitude of the geoid can be predicted. The corresponding matches to observed plate tectonic velocities are more model dependant and vary from 1/4 to 2/3, when the selection criterium used tries to reduce the misfit C_N with geoid. Even better results were computed for $\vec{\nabla}.\vec{v}$ when the selection procedure directly optimizes the fit C_v for the velocities: it climbed to 82%. One final impression emerges from Table 1: the best match for the geoid occurs when the surface velocity is by construction identical to that of plate tectonics ("With Imposed Velocities" column) or turns out to approach it very closely ("class 2" column). The above statements about the root mean square of the distance between predicted and observed geoid or divergence of surface velocities are somewhat severe. A more encouraging conclusion can be drawn by contemplat-

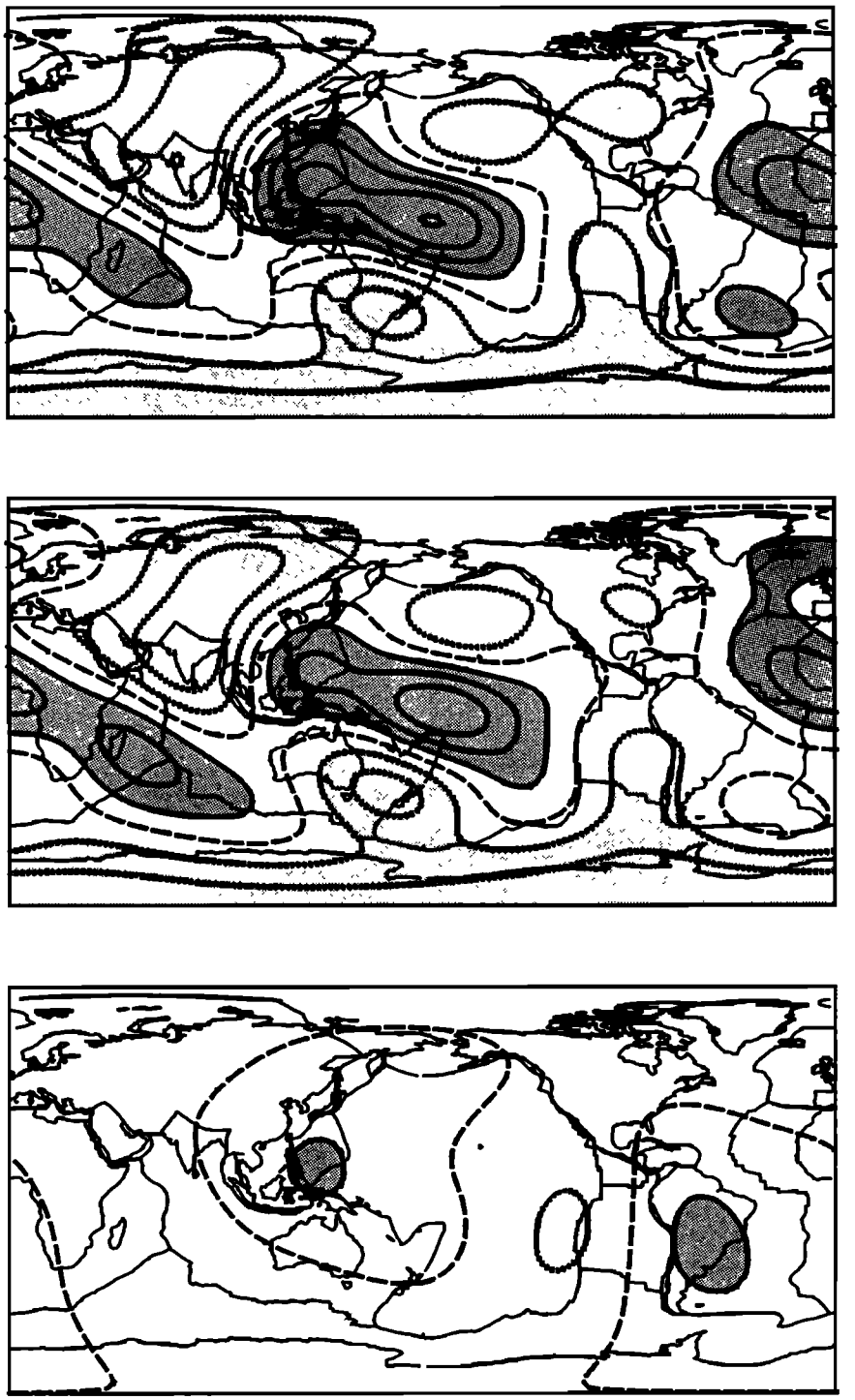

Fig. 15. Predicted geoid (top map) for the solution corresponding to the best set of parameters in Figure 14. The lower maps like in Figure 13 depict separately the contributions due to internal loads and to imposed surface velocities.

ing predicted and observed maps which exhibit striking similarities and by stating the values of correlation coefficients which are often found close to the 90% confidence level. More optimistic conclusions have sometimes been derived on the basis of similar dynamic models, but using different density sources [*Richards and Hager*, 1986]. The major discrepancy seems to arise from using an unpublished lower mantle tomography by Comer and Clayton with a stronger zonal degree 2 term than that of Dziewonski. This last statement is corroborated by a comparison of the geoid respectively induced by these two tomography models [*Hager et al.*, 1985, Figure 3]. It is further supported by a computation we performed, where only the lower mantle tomography of degrees $l = 2$ and $l = 3$ [*Dziewonski*, 1984] and the slabs are considered as internal loads, i.e., ignoring up-

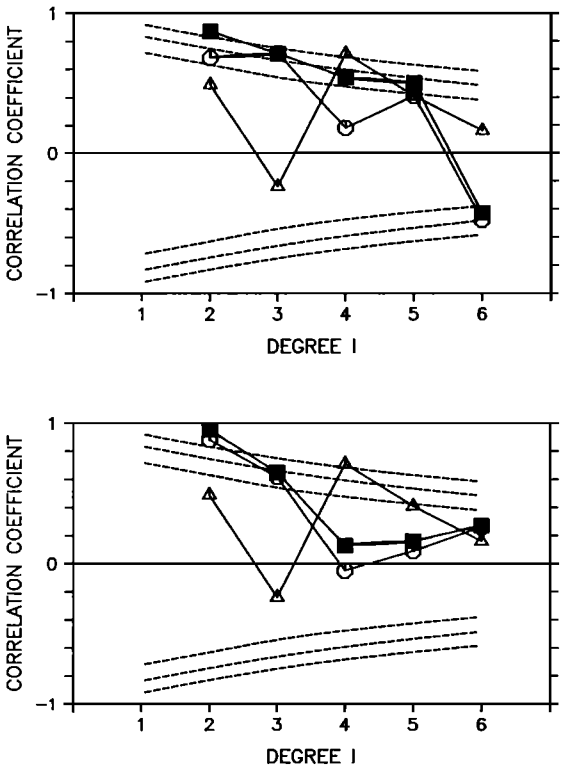

Fig. 16. Correlation coefficients between observed and predicted geoids for spherical harmonics degrees 2 to 6. The top graph is for an Earth model with physical interface at 650 km, whereas the bottom graph implies a chemical interface. The solid squares, open circles, and triangles correspond respectively to the three maps of Figures 13 and 15, i.e., to the total geoid, its component generated by internal loads alone, and its component generated by imposed surface velocities alone.

TABLE 1. Best fit, Given in Percent, Between Observed and Computed Geoid or Surface Velocity Divergence For Six Types of Earth Models

	Class 1	Class 2	With Imposed Velocities
Physical Interface			
Geoid	24%	32%	34%
Velocity	44%	56%	
Chemical Interface			
Geoid	24%	32%	32%
Velocity	26%	64%	

per mantle tomography. This approach, similar to that of *Hager et al.* [1985] yields 35% of the observed geoid, a performance very similar to those found in Table 1.

The second and last lesson to draw from this study concerns the overall viscosity structure of the mantle. Class 1 solutions yield a viscosity profile which continuously increases beneath the lithosphere, with a contrast about 2 orders of magnitude. This result must be compared with conclusions from other observations. On the one hand it contradicts the postglacial rebound studies, which predict a more moderate viscosity increase. On the other hand, even with physical interface, it suggests a partial decoupling between the upper and lower mantle circulation. The former is more vigorous, but not fully distinct from the latter which evolves much more slowly [*Davies*, 1977]. In other words the picture of two-layer mantle convection, which is compatible with the presence of two geochemical reservoirs, could be replaced by a one-layer system with a much larger residence time for lower mantle trajectories. The class 1 solutions also select amplitudes for the density anomalies close to standard expectations. In particular, the role of upper mantle heterogeneities defined by tomography turns out to be important. Our class 2 solutions yield a quite uniform mantle viscosity except for a stiff layer at the bottom of the upper mantle. Such solutions could mimic an Earth structure with 2 stages of convection. Even if one may expect this stiff boundary to make the slab penetration into the lower mantle difficult, we consider that these solutions cannot be discarded without further analysis. The case with a chemical interface is physically simple: the lower mantle circulation generates practically no topography and velocity at the Earth's surface, but merely contributes to the geoid. The slabs, which, for this class of solutions, turn out to have marked density contrasts, constitute the main driving forces for the surface circulation and produce strong positive geoid components. When the mantle circulation is excited by mass anomalies and fits the observed plate motion, the derived viscosity profile is somewhat different from both the class 1 and class 2 solutions.

In conclusion this study has illustrated the importance of considering both the gravity and the surface velocity fields to constrain the internal dynamics of the Earth. Even if internal loads suggested by the emerging tomographic data sets still contain sizable uncertainties, the global physical understanding is satisfactory. However, our analysis calls for some caution, as the choice of a coarse radial viscosity structure remains somewhat open.

Acknowledgments. This work was supported in part by Centre National de la Recherche Scientifique (CNRS, ATP télédétection) and Institut National des Sciences de l'Univers (INSU). Contribution n°5 of the INSU-DBT program: theme of global coupling.

References

Clayton, R. W., and R. P. Comer, A tomographic analysis of mantle heterogeneities from body wave travel times, *Eos Trans. AGU*, *62*, 776, 1983.

Creager, K. C., and T. H. Jordan, Slab penetration into the lower mantle, *J. Geophys. Res.*, *89*, 3031-3044, 1984.

Davies, G. F., Whole-mantle convection and plate tectonics, *Geophys. J. R. Astron. Soc.*, *49*, 459-486, 1977.

Dziewonski, A. M., Mapping the lower mantle: determination of lateral heterogeneity in P vel-

ocity up to degree and order 6, *J. Geophys. Res.*, *89*, 5929-5952, 1984.

Dziewonski, A. M., and D. L. Anderson, Preliminary Reference Earth Model (PREM), *Phys. Earth Planet. Inter.*, *25*, 297-356, 1981.

Dziewonski, A. M., and J. H. Woodhouse, Seismic tomography and the scale of mantle convection, *Eos Trans. AGU*, *69*, 494, 1988.

Forsyth, D. W., and S. Uyeda, On the relative importance of the driving forces of plate motion, *Geophys. J. R. Astron. Soc.*, *43*, 163-200, 1975.

Forte, A. M., and W. R. Peltier, Plate tectonics and aspherical Earth structure: The importance of poloidal-toroidal coupling, *J. Geophys. Res.*, *92*, 3645-3679, 1987.

Hager, B. H., and R. J. O'Connell, Kinematic models of large-scale flow in the Earth's mantle, *J. Geophys. Res.*, *84*, 1031-1048, 1978.

Hager, B. H., Subducted slabs and the geoid: Constraints on mantle rheology and flow, *J. Geophys. Res.*, *89*, 6003-6016, 1984.

Hager, B. H., and M. A. Richards, The generation of long-wavelength geoid anomalies: Implications for mantle structure and dynamics, *Terra Cognita*, *4*, 247, 1984.

Hager, B. H., R. W. Clayton, M. A. Richards, R. P. Comer and A. M. Dziewonski, Lower mantle heterogeneity, dynamic topography, and the geoid, *Nature*, *313*, 541-545, 1985.

Kaula, W. M., Tests of satellite determinations of the gravity field against gravimetry and their combination, *Publ. 509*, Inst. of Geophys. and Planet. Phys., Univ. of Calif., Los Angeles, 1966.

Lago, B., and M. Rabinowicz, Admittance for a convection in a layered spherical shell, *Geophys. J. R. Astron. Soc.*, *77*, 461-482, 1984.

Nataf, H. C., I. Nakanishi and D. L. Anderson, Measurements of mantle wave velocities and inversion for lateral heterogeneities and anisotropy. 3: Inversion, *J. Geophys. Res.*, *91*, 7261-7307, 1987.

Press, F., Earth models consistent with geophysical data, *Phys. Earth Planet. Inter.*, *3*, 3-22, 1970.

Ricard, Y., L. Fleitout and C. Froidevaux, Geoid heights and lithospheric stresses for a dynamic Earth, *Ann. Geophys., Gauthier Villars*, *2*, 267-286, 1984.

Ricard, Y., B. Hannetelle and L. Fleitout, Earth seismic tomography, geoid and surface topography, E.U.G., *Terra cognita*, *5*, 143, 1985.

Ricard, Y., C. Froidevaux and L. Fleitout, Global plate motion and the geoid: A physical model, *Geophys. J.*, *93*, 477-484, 1988.

Richards, M. A., and B. H. Hager, Geoid anomaly in a dynamic Earth, *J. Geophys. Res.*, *89*, 5987-6002, 1984.

Richards, M. A., and B. H. Hager, The Earth's geoid and the large-scale structure of mantle convection, in *Proceedings of the NATO Advanced Study Institute: Physics of Planets*, University of Newcastle Upon Tyne, 9-20 April 1985.

Richardson, R. M., C. S. Solomon and N. H. Sleep, Tectonic stresses in the plates, *Rev. Geophys.*, *17*, 981-1019, 1979.

Sumino, Y., and O. L. Anderson, Elastic constants of minerals, in *Handbook of Physical properties of Rocks*, Vol. III, edited by R. S. Carmichael, 39-138, CRC Press, Boca Raton, Fla., 1984.

Tanimoto, T., The Backus-Gilbert approach to the three-dimensional structure in the upper mantle: SH and SV velocity, *Geophys. J. R. Astron. Soc.*, *84*, 49-70, 1986.

Woodhouse, J. H., and A. M. Dziewonski, Mapping the upper mantle: Three-dimensional modeling of Earth structure by inversion of seismic waveforms, *J. Geophys. Res.*, *89*, 5953-5986, 1984.

Wu, P., and W. R. Peltier, Viscous gravitational relaxation, *Geophys. J. R. Astron. Soc.*, *70*, 435-485, 1982.

Yuen, D. A., R. Sabadini and E. V. Boschi, Viscosity of the lower mantle as inferred from rotational data, *J. Geophys. Res.*, *87*, 10745-10762, 1982.

C. Froidevaux, Y. Ricard, and C. Vigny Département de Géologie, Ecole Normale Supérieure, 24, rue Lhomond, 75231 Paris Cedex 05.

(Received January 6, 1988;
revised November 28, 1988;
accepted March 2, 1989.)